



Temperature and nickel substitution effects on the phase transitions in the $\text{Sr}_2\text{Zn}_{1-x}\text{Ni}_x\text{WO}_6$ ($0 \leq x \leq 1$) double perovskite

Bouchaib Manoun ^{a,*}, F. Mirinioui ^a, Y. Tamraoui ^a, A. Solhy ^b, Wenge Yang ^{c,d}, P. Lazor ^e

^a Univ Hassan 1^{er}, Laboratoire des Sciences des Matériaux, des Milieux et de la Modélisation (LS3M), 25000, Khouribga, Morocco

^b Center for Advanced Materials (CAM), Mohammed VI Polytechnic University, Lot 660 Hay Moulay Rachid, 43150, Ben Guerir, Morocco

^c High Pressure Science and Technology Advanced Research (HPSTAR), Shanghai, 201203, PR China

^d High Pressure Synergetic Consortium (HPSyNC), Geophysical Laboratory, Carnegie Institution of Washington, Argonne, IL, 60439, USA

^e Department of Earth Sciences, Uppsala University, SE-752 36, Uppsala, Sweden



HPSTAR
266-2016

ARTICLE INFO

Article history:

Received 5 June 2016

Received in revised form

23 July 2016

Accepted 26 July 2016

Available online 30 July 2016

Keywords:

$\text{Sr}_2\text{Zn}_{1-x}\text{Ni}_x\text{WO}_6$ double perovskite

Crystal structure

Phase transitions

X-ray diffraction

Raman spectroscopy

ABSTRACT

$\text{Sr}_2\text{Zn}_{1-x}\text{Ni}_x\text{WO}_6$ solid solutions (with $0 \leq x \leq 1$) have been synthesized by solid-state reactions, and characterized by X-Ray diffraction and Raman spectroscopy. The X-Ray powder diffraction (XRD) data at room temperature shows a systematical change of structure vs. nickel content: the compound adopts a monoclinic phase with a $P2_1/n$ space group with $0 \leq x \leq 0.18$, a tetragonal structure with a $I4/m$ space group with $x = 0.25$, and a tetragonal structure with a $I4/mmm$ space group with $0.5 \leq x \leq 1$. Further in-situ Raman study at elevated temperature (up to 555 °C) shows the pristine monoclinic phase ($0 \leq x \leq 0.18$) follows the phase path: monoclinic ($P2_1/n$) → tetragonal ($I4/m$) → tetragonal ($I4/mmm$) → cubic ($Fm\bar{3}m$); for the compound $\text{Sr}_2\text{Zn}_{0.75}\text{Ni}_{0.25}\text{WO}_6$, it involves later two phase transitions as tetragonal ($I4/m$) → tetragonal ($I4/mmm$) → cubic ($Fm\bar{3}m$); and for the $0.5 \leq x \leq 1$ compounds, only one phase transition $I4/mmm$ to $Fm\bar{3}m$ was observed. The combined investigation of composition and temperature provides us a complete understanding of chemical substitution and temperature effect on structural phase transition.

© 2016 Elsevier B.V. All rights reserved.

1. Introduction

Double perovskites with the general formula $A_2B'B''O_6$ have attracted a lot of attention in recent years because of their exotic physical properties such as superconductivity [1,2], dielectricity [3,4] and magnetoresistivity [5]. A rich variety of structures is found in double perovskites with different chemical compositions and/or temperatures [6,7].

The intrinsic tunneling-type colossal magneto-resistance (CMR) phenomenon was discovered in the double perovskite $\text{Sr}_2\text{FeMoO}_6$ at room temperature, which may have applications on the detection of magnetic fields such as for magnetic memory devices. Solid state chemists and physicists became interested in studying other substituted phases of stoichiometry $A_2B'B''O_6$ (A = alkali earths, B' , B'' = transition metals) [8,9].

Over the preceding decade it has been established that the structural and magnetic properties of the ordered double

perovskites $A_2B'B''O_6$ can be systematically tuned by altering the number of d-electrons of the B-site cation or the size of the cations. These substitutions can result in significant structural distortions which, in turn, have a critical influence on the electric and magnetic properties of these oxides [10–12].

After extensive studies on other members of the $A_2B'B''O_6$ family, it is found that the presence of the colossal magnetoresistance is a common feature for some of them. Thus, large intragrain (bulk) CMR above room temperature has been described in double perovskites with different A cations, such as $\text{Ba}_2\text{FeMoO}_6$ [13] or $\text{Ca}_2\text{FeMoO}_6$ [14], or different B'' from second and third-row transition metals like $\text{Sr}_2\text{FeReO}_6$ [15].

Recently, several research groups have studied series $\text{Sr}_2\text{MW}_2\text{O}_6$ materials (M = Ni, Cu, Mg, Co, Zn, Ca) [16,17]. The structure of Sr_2NiWO_6 crystal, at room temperature has been reported as cubic phase by Zhao et al. [11], but was described by Daisuke Iwanaga et al. [18], Gateski et al. [16] and S.Z. Tian et al. [19] as tetragonal phase with $I4/m$ space group. For Sr_2ZnWO_6 compound, many structures are proposed at room temperature too, such as tetragonal by Kupriyanov and Fesenko [20], monoclinic $I2/m$ by Reinen et al. [21], and monoclinic $P2_1/n$ by Gateski et al. [16].

* Corresponding author.

E-mail address: manounb@gmail.com (B. Manoun).

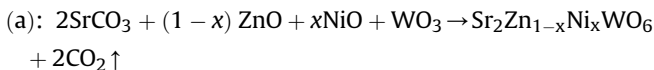
The high temperature Raman spectroscopy studies of the phase transitions in Sr_2ZnWO_6 and Sr_2NiWO_6 double perovskite oxides were investigated by Manoun et al. recently [22,23], they found two phase transitions, from $P2_1/n$ to $I4/m$ around 80°C and from $I4/m$ to $Fm\bar{3}m$ at 480°C for Sr_2ZnWO_6 , and a one phase transition from $I4/m$ to $Fm\bar{3}m$ around 300°C for Sr_2NiWO_6 .

As Sr_2ZnWO_6 and Sr_2NiWO_6 can be synthesized together as solid solution, we are reporting here the structural determination and phase transition behavior of $\text{Sr}_2\text{Zn}_{1-x}\text{Ni}_x\text{WO}_6$ ($0 \leq x \leq 1$) with varied Ni content and temperature with X-ray diffraction and Raman spectroscopy. We discovered four stable structural phases ($P2_1/n$, $I4/m$, $I4/mmm$, and $Fm\bar{3}m$) at different Ni content and temperature range, which provides key information on the structural stability and phase transition mechanism.

2. Experimental

2.1. Synthesis and characterization

Phases of nominal compositions $\text{Sr}_2\text{Zn}_{1-x}\text{Ni}_x\text{WO}_6$ ($0 \leq x \leq 1$) were synthesized by conventional high-temperature solid-state reaction. Stoichiometric amounts of high purity (99.9%) SrCO_3 , ZnO , NiO and WO_3 according to the equation (a) were intimately ground and heated in air at 600°C for 12 h to decompose the carbonates. The powder samples were ground again and heated in air at 900°C for 24 h. The obtained product was heated at 1100°C for 24 h with intermittent grinding.



2.2. XRD measurements

The final products of $\text{Sr}_2\text{Zn}_{1-x}\text{Ni}_x\text{WO}_6$ ($0 \leq x \leq 1$) have been controlled by X-ray powder diffraction analysis. The analysis of powders by X-ray diffraction showed SrWO_4 impurity with low intensity. The structural refinements were undertaken from the powder data. Diffraction data were collected at room temperature on a D2 PHASER diffractometer, with the Bragg–Brentano geometry, using $\text{CuK}\alpha$ radiation ($\lambda = 1.5418\text{\AA}$) with 30 kV and 10 mA. The XRD patterns were scanned through 2θ range $15\text{--}100^\circ$ with stepsize of 0.01° . The full pattern refinements were carried out by means of the Rietveld method using the Fullprof program [24] integrated in Winplotr software [25]. The Rietveld refinement of the observed powder XRD data is initiated with scale and background parameters and successively other profile parameters are included. The background is fitted with a fifth order polynomial. The peak shape is fitted with a pseudo-Voigt profile function. After an appreciable profile matching the atomic position parameters and isotropic atomic displacement parameters of individual atoms were also refined.

2.3. Raman spectroscopy

The Raman spectroscopy measurements were carried out in the Department of Earth Sciences, Uppsala University [26,27]. The key system components include a high-throughput, single stage imaging spectrometer (HoloSpec f/1.8i, Kaiser Optical Systems, Inc.) equipped with a holographic transmission grating and thermoelectrically cooled two-dimensional multichannel CCD detector (Newton, Andor Technology, 1600×400 pixels, thermoelectrically cooled down to -60°C), a diode-pumped laser (Cobolt AB, 532.42

nm , 150 mW), and an optical imaging system (magnification $20 \times$, spatial resolution $\sim 1\text{ }\mu\text{m}$). Two holographic notch filters (Kaiser Optical Systems, Inc.) blocked the Rayleigh line. The spectrometer was calibrated by fluorescence lines of a neon lamp. Non-polarized Raman spectra were collected in the back-scattering geometry, in the range of $40\text{--}1680\text{ cm}^{-1}$, at a resolution of about 3 cm^{-1} . Accuracy and precision of spectral measurements, as estimated from the wavelength calibration procedure and peak fitting results, were 1.5 and $0.1\text{--}0.4\text{ cm}^{-1}$, respectively. The acquisition time varied from 30 s to 5 min.

Heating was accomplished by using a mica insulated band heater (DuraBand, Tempco Electric heater Corporation) mounted around the sample ceramic holder and connected to a variac transformer. Temperature changes during the heating/cooling cycles were induced and controlled by adjusting the transformer's voltage ($0\text{--}240\text{ V}$) and monitored with an accuracy of $\pm 1^\circ\text{C}$ by the K-type thermocouple adjacent to the sample. During the spectral acquisitions, temperatures were stabilized to within 1 and 3°C , for the low and high temperature measurements, respectively.

3. Results and discussions

3.1. Structure determination and description of the structure

The X-ray powder diffraction patterns of $\text{Sr}_2\text{Zn}_{1-x}\text{Ni}_x\text{WO}_6$ ($0 \leq x \leq 1$) in the $15\text{--}100^\circ 2\theta$ range are shown in Fig. 1, where the phase transition from monoclinic to tetragonal is clearly shown. The crystal structures of seven different Ni contents were refined from the high resolution XRD patterns acquired at room temperature. The structures of $\text{Sr}_2\text{Zn}_{1-x}\text{Ni}_x\text{WO}_6$ with $0 \leq x \leq 0.18$ were determined as monoclinic phase with space group $P2_1/n$, the $\text{Sr}_2\text{Zn}_{0.75}\text{Ni}_{0.25}\text{WO}_6$ as the tetragonal phase with space group $I4/m$ and the $\text{Sr}_2\text{Zn}_{1-x}\text{Ni}_x\text{WO}_6$ ($0.25 < x \leq 1$) as the tetragonal phase with space group $I4/mmm$. The data analysis revealed the presence of minor impurities of SrWO_4 , the concentration of SrWO_4 is between 2% and 7% except for $x = 0.25$ where the percentage is around 12%. The composition dependence of the lattice parameters is illustrated in Fig. 2. Due to the smaller ionic radius of Ni^{2+} (0.69\AA) compared to Zn^{2+} (0.74\AA) [28], there is a gradual decrease in cell parameters as substituting Zn^{2+} by Ni^{2+} . This smaller size of Ni^{2+} is also responsible for the tetragonal and monoclinic distortion when Zinc is substituted by Nickel.

The Rietveld refinements of the data were performed with the program FullProf [24], and the results are listed in Table 1. The refined atomic coordinates for $\text{Sr}_2\text{Zn}_{1-x}\text{Ni}_x\text{WO}_6$ ($0 \leq x \leq 1$) compositions in the tetragonal and monoclinic systems are given in Table 2.

The structure refinements were performed with space group $P2_1/n$ (SG #14) for compounds $\text{Sr}_2\text{Zn}_{1-x}\text{Ni}_x\text{WO}_6$ ($0 \leq x \leq 0.18$) with starting model from Ref. [29]. In this model Sr^{2+} , $\text{Zn}^{2+}/\text{Ni}^{2+}$ and W^{6+} are placed at Wyckoff positions $4e(x, y, z)$, $2b(0, 0, 1/2)$ and $2a(0, 0, 0)$, respectively; and the oxygen atoms are placed at three different positions $4e(x, y, z)$. The $\text{Sr}_2\text{Zn}_{0.75}\text{Ni}_{0.25}\text{WO}_6$ was refined with space group $I4/m$ (SG #87) and starting model from Ref. [30] where Sr^{2+} , $\text{Zn}^{2+}/\text{Ni}^{2+}$ and W^{6+} are placed at $4d(0, 1/2, 1/4)$, $2a(0, 0, 0)$ and $2b(0, 0, 1/2)$ positions, respectively; and the oxygens at $4e(0, 0, z)$ and $8h(x, y, 0)$ sites. Finally for the compounds $\text{Sr}_2\text{Zn}_{1-x}\text{Ni}_x\text{WO}_6$ ($0.5 \leq x \leq 1$), the refinement of the structure was done with the space group $I4/mmm$ (SG #139), in this model taken from Ref [31], and the Sr^{2+} , $\text{Zn}^{2+}/\text{Ni}^{2+}$ and W^{6+} are placed at $4d(0, 1/2, 3/4)$, $2a(0, 0, 0)$ and $2b(0, 0, 1/2)$ respectively; the oxygen atoms at $4e(0, 0, z)$ and $8h(x, y, 1/2)$. The various inter-atomic distances for $\text{Sr}_2\text{Zn}_{1-x}\text{Ni}_x\text{WO}_6$ ($0 \leq x \leq 1$) compositions in the monoclinic and tetragonal structures are given in Tables 3 and 4.

The excellent agreement between observed and refined XRD

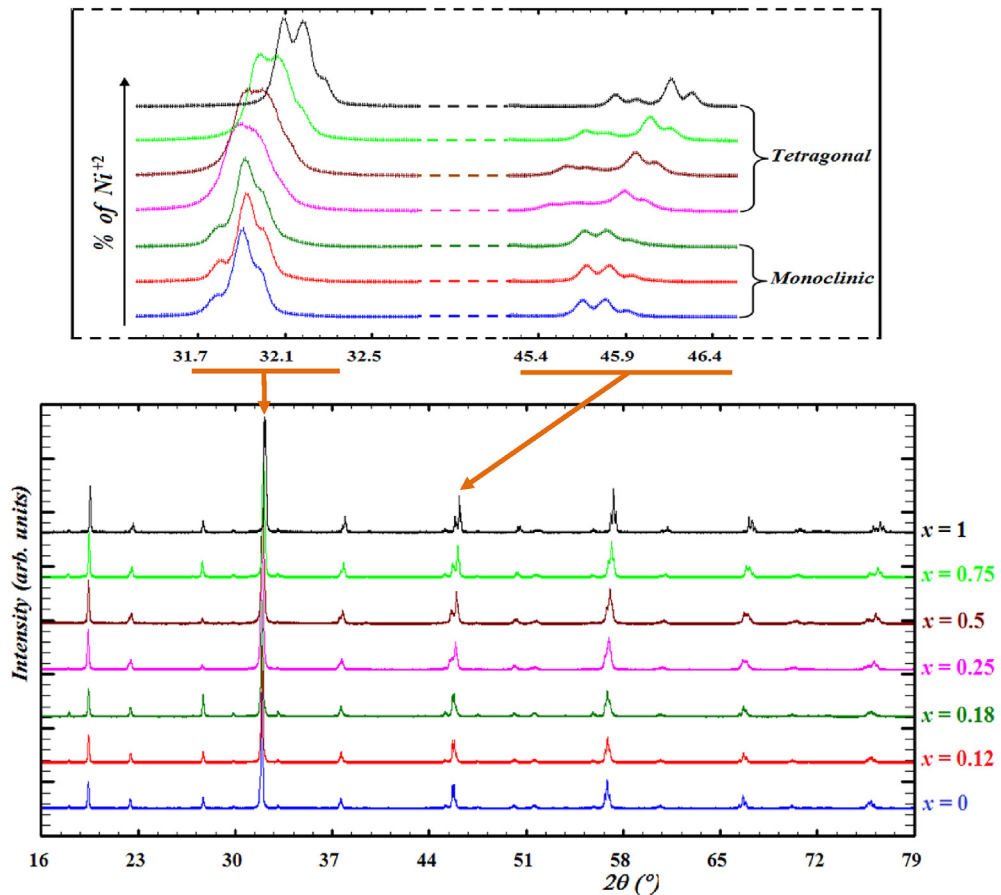


Fig. 1. X-ray powder diffraction patterns for $\text{Sr}_2\text{Zn}_{1-x}\text{Ni}_x\text{WO}_6$ ($0 \leq x \leq 1$).

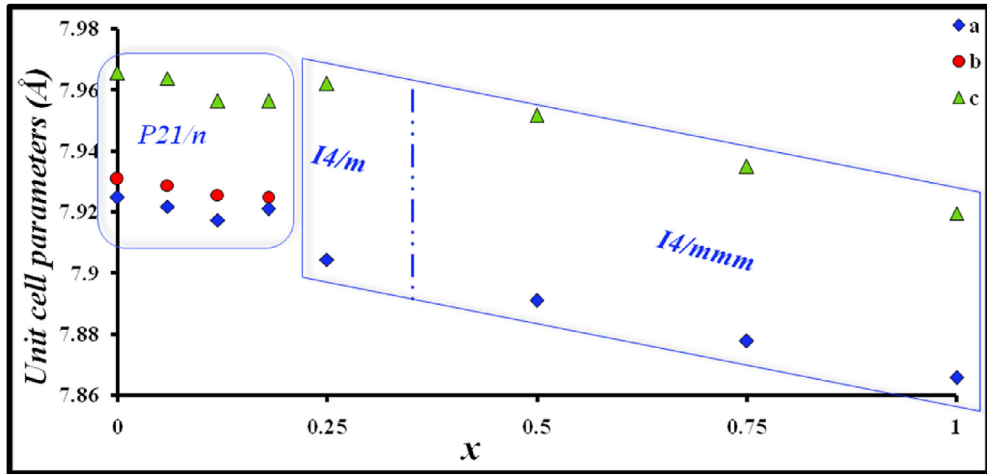


Fig. 2. Variation of the lattice parameters as a function of composition for the series $\text{Sr}_2\text{Zn}_{1-x}\text{Ni}_x\text{WO}_6$ ($0 \leq x \leq 1$). The a values in the tetragonal cells and the a and b values in the monoclinic cells have been multiplied by $2^{1/2}$ for clarity. The monoclinic to tetragonal ($I4/m$) transition is observed between $x = 0.18$ and $x = 0.25$, the tetragonal ($I4/m$) to tetragonal ($I4/mmm$) transition is observed between $x = 0.25$ and $x = 0.5$.

profiles of the monoclinic structure ($P2_1/n$) for $\text{Sr}_2\text{Zn}\text{WO}_6$, tetragonal structure ($I4/m$) for $\text{Sr}_2\text{Zn}_{0.75}\text{Ni}_{0.25}\text{WO}_6$ and tetragonal structure ($I4/mmm$) for $\text{Sr}_2\text{Ni}\text{WO}_6$ are illustrated in Fig. 3.

The atomic projections along (001) direction of the monoclinic ($P2_1/n$), tetragonal ($I4/m$) and tetragonal ($I4/mmm$) phases of $\text{Sr}_2\text{Zn}_{0.94}\text{Ni}_{0.06}\text{WO}_6$, $\text{Sr}_2\text{Zn}_{0.75}\text{Ni}_{0.25}\text{WO}_6$ and $\text{Sr}_2\text{Zn}_{0.25}\text{Ni}_{0.75}\text{WO}_6$ respectively are shown in Fig. 4. The rotation of the octahedron

induced by increasing substitution of Zn^{+2} by Ni^{+2} transforms the monoclinic ($P2_1/n$) structure for ($0 \leq x \leq 0.18$) to the tetragonal structure ($I4/m$) for ($x = 0.25$) and finally to the tetragonal structure ($I4/mmm$) for ($0.5 \leq x \leq 1$).

The examination of crystallographic parameters indicates that the $(\text{Zn}/\text{Ni})^{2+}$ and W^{6+} are octahedrally coordinated with the oxygen atoms. For $P2_1/n$ ($0 \leq x \leq 0.18$): $(\text{Zn}/\text{Ni})\text{O}_6$ and WO_6 are

Table 1

Details of Rietveld refinement parameters of the monoclinic and tetragonal compositions for $\text{Sr}_2\text{Zn}_{1-x}\text{Ni}_x\text{WO}_6$ ($0 \leq x \leq 1$).

Composition	$x = 0$	$x = 0.06$	$x = 0.12$	$x = 0.18$	$x = 0.25$	$x = 0.5$	$x = 0.75$	$x = 1$
Wavelength (Å)	$\lambda_{K\alpha 1} = 1.5406$							
Step scan increment ($^{\circ}2\theta$)	0.01623	0.01623	0.01623	0.01623	0.01623	0.01623	0.01623	0.01623
2θ range ($^{\circ}$)	15–100	15–100	15–100	15–100	15–100	15–100	15–100	15–100
Program	FULLPROF							
Zero point ($^{\circ}2\theta$)	0.0337 (1)	-0.0092 (8)	0.0132 (7)	0.0158 (10)	-0.0170 (7)	0.0180 (5)	0.0343 (3)	0.0538 (3)
Pseudo-Voigt function PV = $\eta L + (1 - \eta) G$	$\eta = 0.705$ (6)	$\eta = 0.851$ (7)	$\eta = 0.719$ (7)	$\eta = 0.707$ (8)	$\eta = 0.612$ (6)	$\eta = 0.755$ (6)	$\eta = 0.737$ (6)	$\eta = 0.605$ (5)
Caglioti parameters	$U = 0.007$ (2)	$U = 0.029$ (3)	$U = 0.057$ (3)	$U = 0.086$ (5)	$U = 0.148$ (6)	$U = 0.071$ (3)	$U = 0.045$ (2)	$U = 0.019$ (1)
	$V = 0.011$ (2)	$V = 0.002$ (2)	$V = -0.025$ (3)	$V = -0.027$ (4)	$V = -0.006$ (4)	$V = 0.007$ (3)	$V = 0.001$ (2)	$V = -0.007$ (1)
	$W = 0.0028$	$W = 0.0037$	$W = 0.0098$	$W = 0.010$ (7)	$W = 0.0093$	$W = 0.0052$	$W = 0.0057$	$W = 0.0058$
(3)	(4)	(5)		(7)	(5)	(1)		(2)
No. of reflections	305	306	306	308	80	61	61	58.5
No. of refined parameter	34	34	34	34	24	22	22	22
Space group	$P2_1/n$	$P2_1/n$	$P2_1/n$	$P2_1/n$	$I4/m$	$I4/mmm$	$I4/mmm$	$I4/mmm$
a (Å)	5.6326 (6)	5.6313 (1)	5.62604 (5)	5.62612 (2)	5.5893 (7)	5.5798 (6)	5.5704 (4)	5.5619 (3)
b(Å)	5.6080 (7)	5.6065 (5)	5.6043 (2)	5.6039 (5)	5.5893 (7)	5.5798 (6)	5.5704 (4)	5.5619 (3)
c(Å)	7.9249 (9)	7.9219 (2)	7.9175 (2)	7.9210 (3)	7.9621 (1)	7.9518 (10)	7.9349 (8)	7.9196 (5)
β°	90.021 (3)	90.01 (6)	89.98 (6)	89.98 (11)				
V (Å ³)	250.33 (5)	250.11 (7)	249.64 (7)	249.734 (3)	248.74 (6)	247.57 (5)	246.21 (4)	244.99 (2)
Z	2	2	2	2	2	2	2	2
Atom number	4	5	5	5	5	5	5	4
R_F/R_B	7.57/4.43	6.17/5.60	6.48/4.90	5.48/5.43	1.84/2.22	2.04/2.72	2.81/3.18	2.69/3.09
R_p/R_{wp}	7.29/10.3	7.50/10.8	8.90/12.5	9.81/13.3	5.07/6.69	5.39/6.93	5.35/7.09	5.11/7.08
cR_p/cR_{wp}	7.30/10.4	7.49/10.8	8.90/12.5	9.82/13.3	5.06/6.69	5.35/6.88	5.33/7.09	5.10/7.11

Table 2

Refined structural parameters for $\text{Sr}_2\text{Zn}_{1-x}\text{Ni}_x\text{WO}_6$ ($0 \leq x \leq 1$).

	Atom	x	y	z	B (Å ²)	Occ
0	W	0	0	0	1.76 (1)	1
	Zn	0	0	0.5	1.92 (2)	1
	Sr	0.0014 (1)	0.5055 (6)	0.2498 (4)	2.33 (2)	2
	O1	0.0527 (6)	0.0183 (4)	0.2397 (1)	0.43 (3)	2
	O2	-0.2418 (3)	0.2417 (5)	-0.0233 (3)	0.43 (3)	2
	O3	0.2136 (6)	0.2312 (1)	-0.0552 (8)	0.43 (3)	2
0.12	W	0	0	0	2.21 (2)	1
	Zn	0	0	0.5	2.22 (8)	0.88
	Ni	0	0	0.5	2.22 (8)	0.12
	Sr	0.0002 (3)	0.4935 (4)	0.2509 (5)	2.75 (5)	2
	O1	-0.04037 (8)	0.0053 (3)	0.2451 (5)	0.07 (1)	2
	O2	-0.2142 (12)	0.2629 (2)	-0.0325 (6)	0.07 (1)	2
	O3	0.2477 (7)	0.2136 (1)	0.0436 (4)	0.07 (1)	2
0.18	W	0	0	0	2.12 (2)	1
	Zn	0	0	0.5	2.01 (9)	0.82
	Ni	0	0	0.5	2.007 (9)	0.18
	Sr	0.0002 (9)	0.4934 (6)	0.2508 (1)	2.75 (6)	2
	O1	-0.0464 (2)	0.0050 (3)	0.2448 (2)	0.07 (1)	2
	O2	-0.2140 (3)	0.2628 (2)	-0.0324 (7)	0.07 (1)	2
	O3	0.2478 (1)	0.2135 (3)	0.0406 (5)	0.07 (1)	2
0.25	W	0	0	0.5	0.39 (2)	1
	Sr	0	0.5	0.25	1.10 (3)	2
	Ni	0	0	0	0.63 (4)	0.25
	Zn	0	0	0	0.63 (4)	0.75
	O1	0	0	0.2695 (9)	1.35 (14)	2
	O2	0.2326 (5)	0.3041 (15)	0	1.35 (14)	4
0.5	W	0	0	0.5	0.37 (5)	1
	Sr	0	0.5	0.75	1.08 (10)	2
	Ni	0	0	0	0.89 (8)	0.5
	Zn	0	0	0	0.89 (8)	0.5
	O1	0	0	0.2644 (10)	2.29 (11)	2
	O2	0.2332 (3)	0.2332 (3)	0.5	2.29 (11)	4
1	W	0	0	0.5	0.48 (2)	1
	Sr	0	0.5	0.75	1.01 (3)	2
	Ni	0	0	0	0.91 (5)	1
	O1	0	0	0.2676 (8)	1.99 (9)	2
	O2	0.2312 (5)	0.2312 (5)	0.5	1.990 (91)	4

connected by O1 and O2 along a and b axis, and by O3 along c-axis. The tilt of the octahedra is observed from the three bond angles (Zn/Ni)-O1-W (165.42°), (Zn/Ni)-O2-W (163.52°) and (Zn/Ni)-O3-W (157.81°) and satisfies the $a^+b^+c^-$ tilt system in Glazer's

Table 3

Selected inter-atomic distances and O-W-O angles for $\text{Sr}_2\text{Zn}_{1-x}\text{Ni}_x\text{WO}_6$ ($0 \leq x \leq 0.18$).

Monoclinic $P2_1/n$	$x = 0$	$x = 0.06$	$x = 0.12$	$x = 0.18$
2(W-O1)	1.9256 (3)	1.9562 (4)	1.9541 (4)	1.9567 (7)
2(W-O2)	1.9303 (2)	1.9272 (2)	1.9205 (3)	1.9194 (4)
2(W-O3)	1.8222 (2)	1.8734 (3)	1.8691 (3)	1.8649 (5)
2(Zn/Ni-O1)	2.0864 (3)	2.0264 (4)	2.0311 (4)	2.0384 (7)
2(Zn/Ni-O2)	2.0610 (2)	2.0981 (3)	2.1019 (3)	2.1028 (5)
2(Zn/Ni-O3)	2.2507 (2)	2.1740 (3)	2.1704 (3)	2.1667 (4)
Sr-O1	2.7487 (3)	2.7442 (2)	2.7456 (6)	2.7495 (2)
Sr-O1	2.8913 (4)	2.8783 (3)	2.8780 (6)	2.8796 (3)
Sr-O1	2.6039 (5)	2.6130 (5)	2.5879 (2)	2.5540 (6)
Sr-O1	3.1228 (3)	3.0201 (5)	3.0401 (3)	3.0741 (4)
Sr-O2	2.9308 (2)	2.8619 (1)	2.8564 (3)	2.8556 (4)
Sr-O2	3.1048 (5)	3.1370 (2)	3.1363 (3)	3.1375 (2)
Sr-O2	2.5141 (3)	2.5132 (1)	2.5108 (2)	2.5113 (3)
Sr-O2	2.6921 (5)	2.7530 (3)	2.7551 (4)	2.7565 (2)
Sr-O3	2.6588 (5)	2.6568 (2)	2.6632 (3)	2.6783 (6)
Sr-O3	2.4539 (4)	2.4764 (2)	2.4868 (2)	2.5031 (3)
Sr-O3	3.1679 (7)	3.1880 (3)	3.1746 (4)	3.1582 (4)
Sr-O3	2.9573 (6)	2.9685 (4)	2.9548 (5)	2.9367 (4)
1*O1-W-O1	180	180	180	180
2*O1-W-O2	99.52 (3)	93.17 (4)	92.78 (4)	92.18 (6)
2*O1-W-O2	80.48 (2)	86.83 (4)	87.22 (4)	87.82 (7)
2*O1-W-O3	84.41 (2)	82.91 (5)	83.88 (4)	85.38 (8)
2*O1-W-O3	95.59 (2)	97.09 (5)	96.12 (4)	94.62 (8)
1*O2-W-O2	180	180	180	180
2*O2-W-O3	93.26 (3)	90.18 (4)	90.08 (3)	90.01 (2)
2*O2-W-O3	86.74 (2)	89.82 (3)	89.92 (3)	89.99 (5)
1*O3-W-O3	180	180	180	180

notation [32], for $I4/m$ ($x = 0.25$): (Zn/Ni)O₆ and WO₆ are connected by O1 along c-axis, and by O2 along a and b axis. (Zn/Ni)-O1-W was 180° indicating no tilt with respect to a- and b-axes. The tilt of the octahedra is observed from the (Zn/Ni)-O2-W bond angle (163.6°); the tilt pattern of the octahedral units satisfies the $a^0a^0c^-$ tilt system in Glazer's notation [32]. For $I4/mmm$ ($0.5 \leq x \leq 1$): (Zn/Ni)O₆ and WO₆ are connected by O1 along c-axis, and by O2 along a and b axes. The tilt pattern of the octahedral units satisfies the $a^0b^+b^+$ tilt system in Glazer's notation [32].

The evolution of the tolerance factor (obtained from the experimental distances) as a function of the composition is a very interesting way to illustrate the phase transitions (Fig. 5). The phase

Table 4Selected inter-atomic distances and O-W-O angles for $\text{Sr}_2\text{Zn}_{1-x}\text{Ni}_x\text{WO}_6$ ($0.25 \leq x \leq 1$).

Tetragonal ($I4/m$)	$x = 0.25$	Tetragonal ($I4/mmm$)	$x = 0.5$	$x = 0.75$	$x = 1$
2•W-01	1.8350 (7)	2•W-01	1.8735 (2)	1.8607 (2)	1.8411 (6)
4•W-02	1.8531 (8)	4•W-02	1.8399 (14)	1.8276 (1)	1.8182 (3)
2•Zn/Ni -01	2.1462 (7)	2•Zn/Ni -01	2.1024 (3)	2.1067 (2)	2.1191 (6)
4•Zn/Ni -02	2.1403 (8)	4•Zn/Ni -02	2.1056 (2)	2.1112 (1)	2.1153 (3)
4•Sr-01	2.7989 (4)	4•Sr-01	2.7922 (3)	2.7879 (2)	2.7845 (3)
4•Sr-02	2.6170 (5)	8•Sr-02	2.8038 (2)	2.79891 (2)	2.7945 (3)
4•Sr-02	3.0142 (6)	1•O1-W-01	180	180	180
1•O1-W-01	180	8•O1-W-02	90	90	90
8•O1-W-02	90	2•O2-W-02	180	180	180
2•O2-W-02	180	4•O2-W-02	90	90	90
4•O2-W-02	90				

transitions from monoclinic $P2_1/n$ to tetragonal $I4/m$ and to tetragonal $I4/mmm$ are clearly illustrated in the Fig. between the compositions 0.18 and 0.25 for transition $P2_1/n \rightarrow I4/m$ and between the composition 0.25 and 0.5 for transition $I4/m \rightarrow I4/mmm$.

3.2. Raman spectroscopy studies

3.2.1. Group theory analysis

Doubles perovskites of the general formula $A_2\text{BB}'\text{O}_6$, with ideal cubic structures will be presented by materials with tolerance factors close to or greater than 1. However, the most interesting and frequent cases are shown by ordered, yet untilted lattices with $Fm\bar{3}m$ symmetry (O_h^5 , No. 225, and Glazer's notation $a^0a^0a^0$) [32]. This configuration allows a classification of the normal modes at the Brillouin zone centre as:

$$\begin{aligned} \Gamma = & A_{1g}(R) + E_g(R) + 2F_{2g}(R) + F_{1g}(s) + 4F_{1u}(IR) + F_{2u}(s) \\ & + F_{1u}(as) \end{aligned}$$

The symmetry analysis of the irreducible representations above indicates that four modes are Raman active (A_g , E_g , $2F_{2g}$), and another four modes are infrared active ($4F_{1u}$). For our compounds, XRD data showed that in this solid solution of doubles perovskites three low symmetries are adopted with increasing the nickel concentration from the small distorted pseudo-cubic $I4/mmm$ (D_{4h}^{17} , No. 139, Glazer's notation $a^0b^+b^+$) to $I4/m$ (C_{4h}^5 , No. 87, Glazer's notation $a^0a^0c^-$), then to a lower symmetry $P2_1/n$ (C_{2h}^4 , No. 14, Glazer's notation $a^+b^+c^-$). According to the factor group analysis [33], twenty-four Raman-active modes, represented as $\Gamma_{P2_1/n}^R = 12A_g + 12B_g$ should be present for the monoclinic composition with system $P2_1/n$. Only nine Raman-active modes can be observed for the tetragonal compositions, represented as $\Gamma_{I4/m}^R = 3A_g + 3B_g + 3E_g$, and $\Gamma_{I4/mmm}^R = 2A_{1g} + A_{2g} + B_{1g} + 2B_{2g} + 3E_g$, for space groups $I4/m$ and $I4/mmm$, respectively. Most of the bands are weak; there are only seven strong bands and they are observed at wavenumbers around 855.76 cm^{-1} , 572.44 cm^{-1} , 447.06 cm^{-1} , 436.63 cm^{-1} , 166.38 cm^{-1} , 151.89 cm^{-1} and 138.17 cm^{-1} for the monoclinic Sr_2ZnWO_6 and four strong bands around 859.88 cm^{-1} , 614.70 cm^{-1} , 140.41 cm^{-1} , 445.26 cm^{-1} for the tetragonal Sr_2NiWO_6 .

Considering the internal vibration modes (v_1 , v_2 , v_5) of the octahedron and the translational modes T and L the irreducible representation for the cubic double perovskite with $Fm\bar{3}m$ as space group can be writing as $\Gamma_{Fm\bar{3}m}^R = v_1(A_{1g}) + v_2(E_g) + v_5(F_{2g}) + T(F_{2g}) + L(F_{1g})(s)$, where the v_1 mode is the symmetric oxygen stretching vibration of W-O in the WO_6 octahedra, appears as a strong peak at higher frequencies $\geq 700 \text{ cm}^{-1}$ [34], the v_2 vibration mode is the asymmetric stretching vibration W-O is located in the range 450 – 600 cm^{-1} , and the O-W-O bending mode labeled as the v_5 mode is expected to occur in the range between 300 and 450 cm^{-1} .

due to the bending mode motion in the WO_6 octahedron [34,35]. The translational lattice modes T are located in the range of frequencies below 300 cm^{-1} , and the mode labeled with L also considered as lattice modes but is silent for the cubic double perovskite. Lowering the symmetry to $I4/mmm$ and $I4/m$ tetragonal system, the irreducible representation of the Raman active modes can be written as $\Gamma = v_1(A_{1g}) + v_2(A_{1g} + B_{1g}) + v_5(B_{2g} + E_g) + T(B_{2g} + E_g) + L(A_{2g} + E_g)$ for the $I4/mmm$ system, and $\Gamma = v_1(A_g) + v_2(A_g + B_g) + v_5(B_g + E_g) + T(B_g + E_g) + L(A_g + E_g)$ for the $I4/m$ system. When the monoclinic structure takes place with $P2_1/n$ as space group only A_g and B_g modes are expected, in this structure the symmetric stretch v_1 exhibits a single band, a doublet for the asymmetric stretching v_2 , and triplet for banding mode v_5 . The irreducible representation can be written as $\Gamma = v_1(A_g + B_g) + v_2(2A_g + 2B_g) + v_5(3A_g + 3B_g) + T(3A_g + 3B_g) + L(3A_g + 3B_g)$. In the studied series the experimentally observed bands for the tetragonal and the monoclinic compositions are shown in Table 5.

In Fig. 6 we show the compatibility relations for the space groups present in the phase-transition sequence: $P2_1/n \rightarrow I4/m \rightarrow I4/mmm \rightarrow Fm\bar{3}m$.

The Raman spectra of $\text{Sr}_2\text{Zn}_{1-x}\text{Ni}_x\text{WO}_6$ ($0 \leq x \leq 1$) recorded at ambient conditions are illustrated in Fig. 7. For all the composition ranges, the observed Raman modes can be classified into three general families of lattice vibrations: Sr⁺ translations, as well as translational and rotational modes of the WO_6 -octahedra, at frequencies below 300 cm^{-1} ; O-W-O bending Vibrations, in the 300 – 500 cm^{-1} region; and W-O stretching modes, at frequencies over 500 cm^{-1} . These frequency families were also observed in double perovskites, such as Sr_2ZnWO_6 [22] and in $\text{Sr}_2\text{ZnTeO}_6$ [36], A_2CoBO_6 ($\text{A} = \text{Sr}$ and Ca , $\text{B} = \text{Te}$ and W) [37].

The analyses of the composition dependence of modes, ration intensity and FWHM of those modes indicate the presence of two phase transitions induced by composition. The composition dependence of the modes is illustrated in Fig. 8 as a function of the nickel content. The modes centered at 436.61 cm^{-1} and 447 cm^{-1} merged at the composition $x = 0.25$ (Fig. 8a), the mode centered at 855.75 cm^{-1} show a remarkable change in slope as a function of the nickel amount indicating the first phase transition from the monoclinic symmetry $P2_1/n$ to the tetragonal symmetry $I4/m$ between $x = 0.18$ et 0.25 (Fig. 8b). The second phase transition from the tetragonal symmetry $I4/m$ to another tetragonal system $I4/mmm$ between $x = 0.25$ and 0.5 (Fig. 8a, b). To better understand the phase transitions induced by composition in the series $\text{Sr}_2\text{Zn}_{1-x}\text{Ni}_x\text{WO}_6$, the relative intensity ratio and FWHM dependence of modes were examined. The behaviors of composition dependence of intensity ratio of the modes are illustrated in Fig. 8(c, d) showing the first and second phase transitions. The monoclinic symmetry is adopted in the composition range between $x = 0$ to 0.18 , then the structure moves to tetragonal symmetry $I4/m$ for $x = 0.25$, and then the

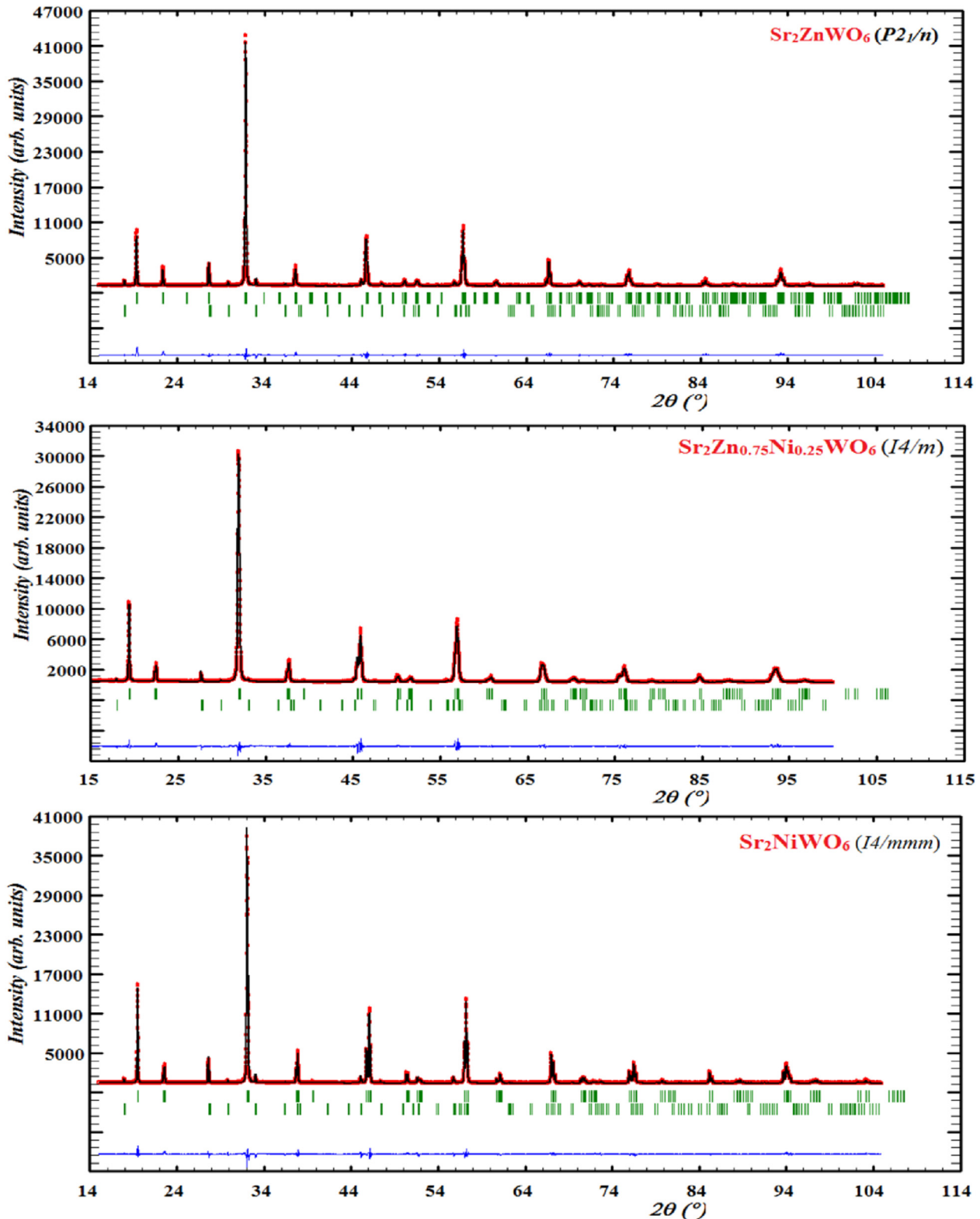


Fig. 3. The Rietveld refinement plots for monoclinic ($P2_1/n$) Sr_2ZnWO_6 , tetragonal ($I4/m$) $\text{Sr}_2\text{Zn}_{0.75}\text{Ni}_{0.25}\text{WO}_6$ and tetragonal ($I4/mmm$) Sr_2NiWO_6 . The upper symbols illustrate the observed data (circles) and the calculated pattern (solid line). The vertical markers show calculated positions of Bragg reflections. The lower curve is the difference diagram.

tetragonal system with $I4/mmm$ as space group is adopted for the composition $x > 0.25$. The FWHM of the translational lattice mode T centered at around 151.89 cm^{-1} and the asymmetric vibration v_5 centered at around 447 cm^{-1} are clearly affected by the monoclinic

($P2_1/n$) \rightarrow tetragonal ($I4/m$) \rightarrow tetragonal ($I4/mmm$) distortion; Fig. 8(e, f) show a clear change in the composition dependence of the FWHM on those modes; all these features are consistent with the Rietveld refinement studies.

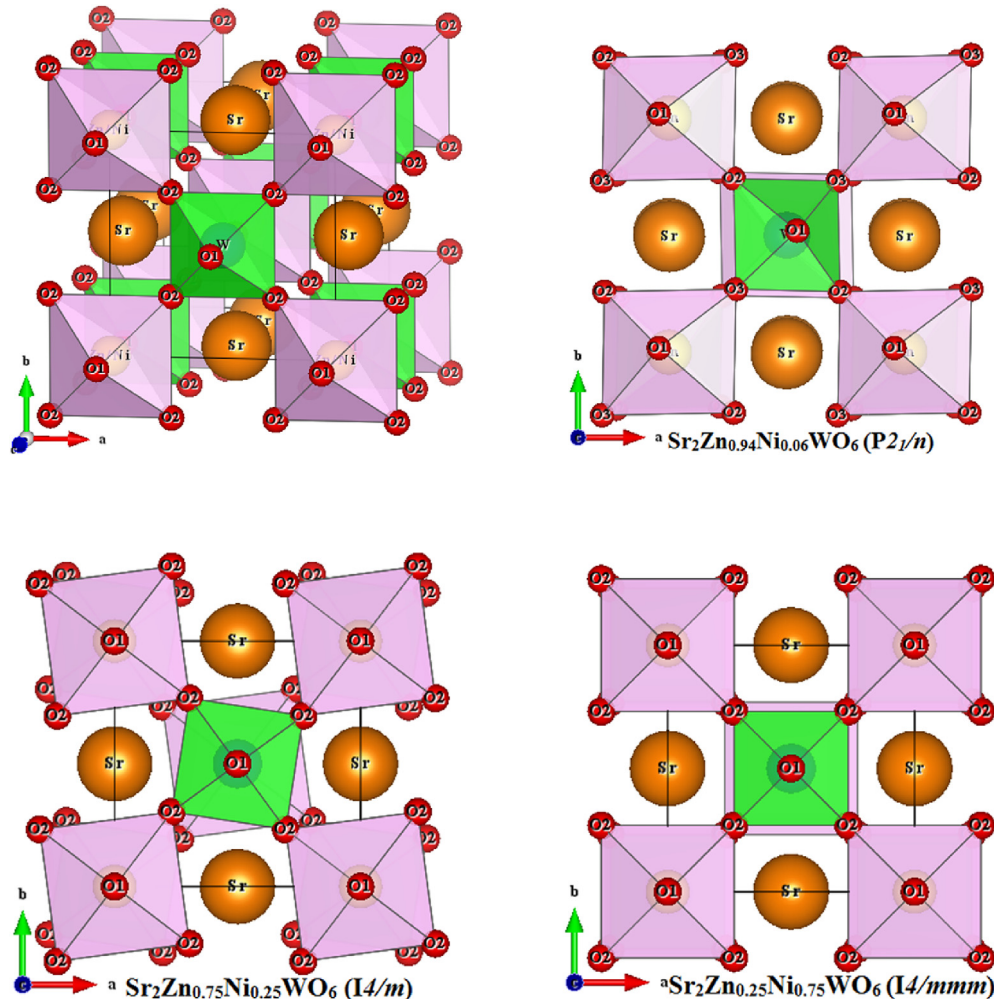


Fig. 4. Illustrations of the effect of tilting of the WO_6 and Ni/ZnO_6 octahedra in the different space group structure in $\text{Sr}_2\text{Zn}_{1-x}\text{Ni}_x\text{WO}_6$.

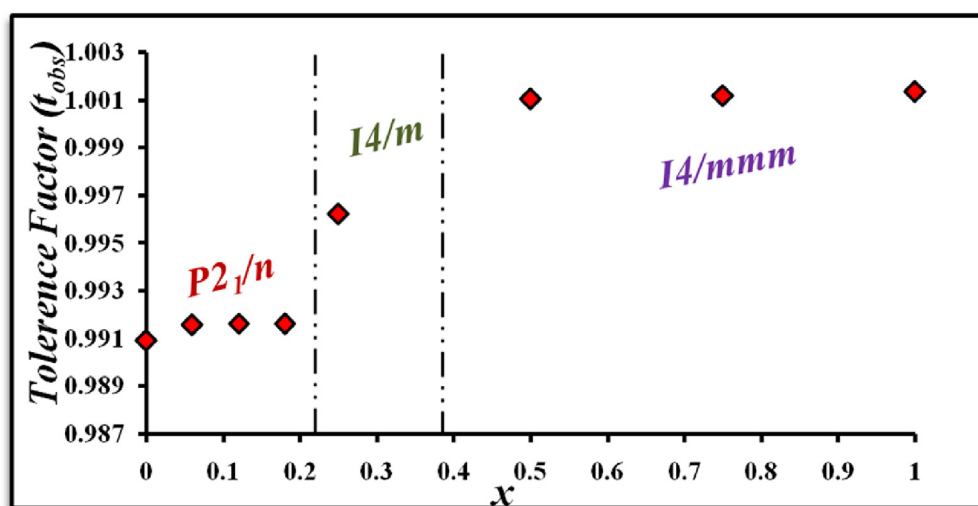


Fig. 5. Observed tolerance factor (obtained from the Rietveld refinements) as a function of the Nickel amount in $\text{Sr}_2\text{Zn}_{1-x}\text{Ni}_x\text{WO}_6$ ($0 \leq x \leq 1$).

Table 5

Raman shifts (in cm^{-1}) for the observed modes in the series $\text{Sr}_2\text{Zn}_{1-x}\text{Ni}_x\text{WO}_6$, with assignment of internal and external modes v_1 , v_2 , v_5 , T, and L.

Assignment	$\text{Sr}_2\text{Zn}\text{WO}_6$ (S.g $P2_1/n$)	$\text{Sr}_2\text{Zn}_{0.94}\text{Ni}_{0.06}\text{WO}_6$ (S.g $P2_1/n$)	$\text{Sr}_2\text{Zn}_{0.88}\text{Ni}_{0.12}\text{WO}_6$ (S.g $P2_1/n$)	$\text{Sr}_2\text{Zn}_{0.82}\text{Ni}_{0.18}\text{WO}_6$ (S.g $P2_1/n$)	$\text{Sr}_2\text{Zn}_{0.75}\text{Ni}_{0.25}\text{WO}_6$ (S.g $I4/m$)	$\text{Sr}_2\text{Zn}_{0.5}\text{Ni}_{0.5}\text{WO}_6$ (S.g $I4/mmm$)	$\text{Sr}_2\text{Zn}_{0.25}\text{Ni}_{0.75}\text{WO}_6$ (S.g $I4/mmm$)	$\text{Sr}_2\text{Ni}\text{WO}_6$ (S.g $I4/mmm$)
T	138.16	137.91	138.02	137.95	136.75	138.23	138.28	140.62
T	151.89	151.23	151.03	149.36	142.61	141.35	141.39	141.95
T	166.38	164.99	164.43	160.3				
v_5	436.63	436.56	436.27	437.22	442.75	442.99	443.1	445.39
v_5	447.06	445.72	445.34	444.73				
v_2	572.44	574.33	590.85	588.63	595.42	601.84	607.77	615.15
v_1	855.76	856.34	856.88	857.41	857.33	857.93	857.85	859.9

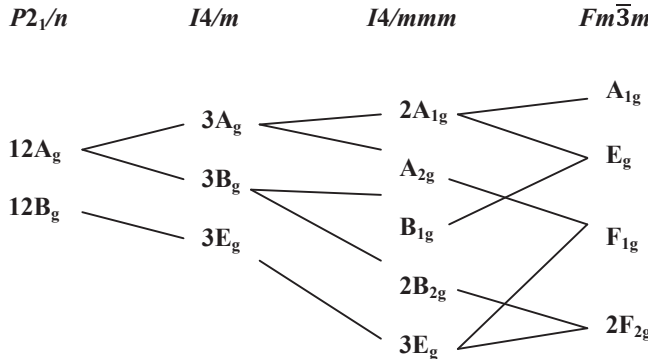


Fig. 6. Correlation diagrams for the Raman-active vibrations in the monoclinic ($P2_1/n$), the tetragonal ($I4/m$), ($I4/mmm$) and the cubic ($Fm\bar{3}m$) phases of $\text{Sr}_2\text{Zn}_{1-x}\text{Ni}_x\text{WO}_6$.

compounds to elevated temperature at ambient pressure and observed the series of phase transitions at varies temperature.

Raman spectra of $\text{Sr}_2\text{Zn}_{1-x}\text{Ni}_x\text{WO}_6$ were collected at elevated temperatures, up to 555 °C. As an example the Raman spectra obtained at several temperatures for $\text{Sr}_2\text{Zn}_{0.88}\text{Ni}_{0.12}\text{WO}_6$, $\text{Sr}_2\text{Zn}_{0.75}\text{Ni}_{0.25}\text{WO}_6$ and $\text{Sr}_2\text{Zn}_{0.25}\text{Ni}_{0.75}\text{WO}_6$ are presented in Fig. 9. The temperature dependence of the modes and of their intensity ratio and FWHM are used as index to show the temperature phase transition.

In previous works, Manoun et al. [22,23] showed that there are two phase transitions induced by temperature at around 80 °C and 480 °C in monoclinic $\text{Sr}_2\text{Zn}\text{WO}_6$ system, only one 300 °C for the tetragonal $\text{Sr}_2\text{Ni}\text{WO}_6$ system.

In the present study, for $\text{Sr}_2\text{Zn}\text{WO}_6$ and $\text{Sr}_2\text{Zn}_{0.94}\text{Ni}_{0.06}\text{WO}_6$ compounds there are three phase transitions with increasing temperature. As shown in Fig. 10(a, b), remarkable changes of

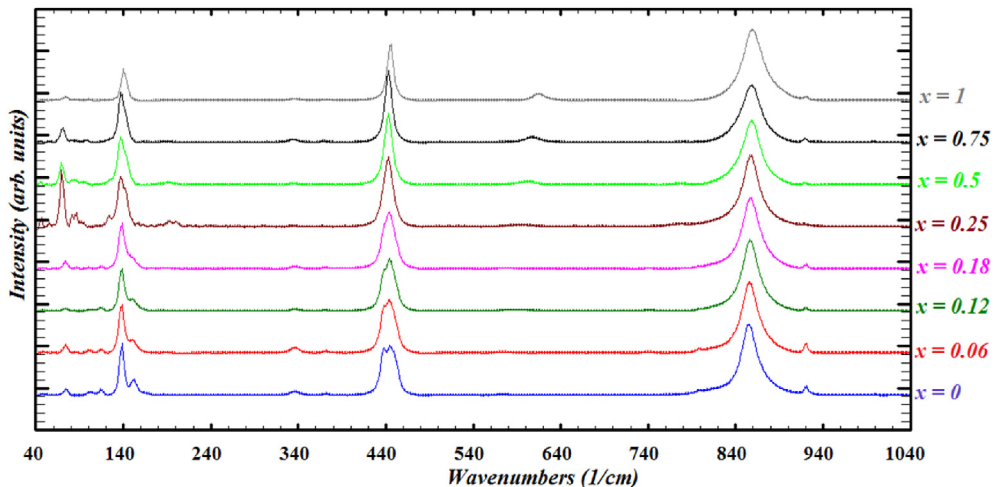


Fig. 7. Raman spectra of $\text{Sr}_2\text{Zn}_{1-x}\text{Ni}_x\text{WO}_6$ ($0 \leq x \leq 1$) recorded at ambient conditions.

3.3. Temperature study of $\text{Sr}_2\text{Zn}_{1-x}\text{Ni}_x\text{WO}_6$ ($0 \leq x \leq 1$) double perovskites

Recently the crystal stability of doubles perovskites at extreme conditions especially at high and low temperatures has attracted a great interest because of those exotic properties. For example, magnetic and superconducting properties at high temperature have been reported [38–41]. Currently lot of studies are devoted on the investigations of the crystal structure and temperature induced phase transitions, many sequence of phase transitions have been reported, such as $I2/m \rightarrow I4/m \rightarrow Fm\bar{3}m$ [42], $P2_1/n \rightarrow I4/m \rightarrow Fm\bar{3}m$ [22], $I4/m \rightarrow I4/mmm$ [16,43].

We have conducted high temperature Raman spectroscopy study in the series of double perovskites oxide $\text{Sr}_2\text{Zn}_{1-x}\text{Ni}_x\text{WO}_6$

Raman modes can be seen in $\text{Sr}_2\text{Zn}_{0.94}\text{Ni}_{0.06}\text{WO}_6$ system as a function of temperature. The modes centered at 136.34 cm^{-1} and 855 cm^{-1} show a break in the slope at around 40 °C, indicating the first temperature phase transition from monoclinic $P2_1/n$ to tetragonal system $I4/m$. Increasing temperature to around 70 °C triggers the second phase transition from $I4/m$ to $I4/mmm$. The third phase transition takes place at around 470 °C.

For $\text{Sr}_2\text{Zn}_{0.88}\text{Ni}_{0.12}\text{WO}_6$, $\text{Sr}_2\text{Zn}_{0.82}\text{Ni}_{0.18}\text{WO}_6$ compounds transitional effects on temperature dependence of the modes, their ratio intensity, and FWHM of the modes are shown in Fig. 11 for $\text{Sr}_2\text{Zn}_{0.88}\text{Ni}_{0.12}\text{WO}_6$ (Fig. 11a, b), and $\text{Sr}_2\text{Zn}_{0.82}\text{Ni}_{0.18}\text{WO}_6$ (Fig. 11c, d) respectively. For the monoclinic $\text{Sr}_2\text{Zn}_{0.88}\text{Ni}_{0.12}\text{WO}_6$, three phases transition are revealed, the first at around 25 °C from $P2_1/n$ system to tetragonal $I4/m$, the second at around 60 °C from $I4/m$ system to

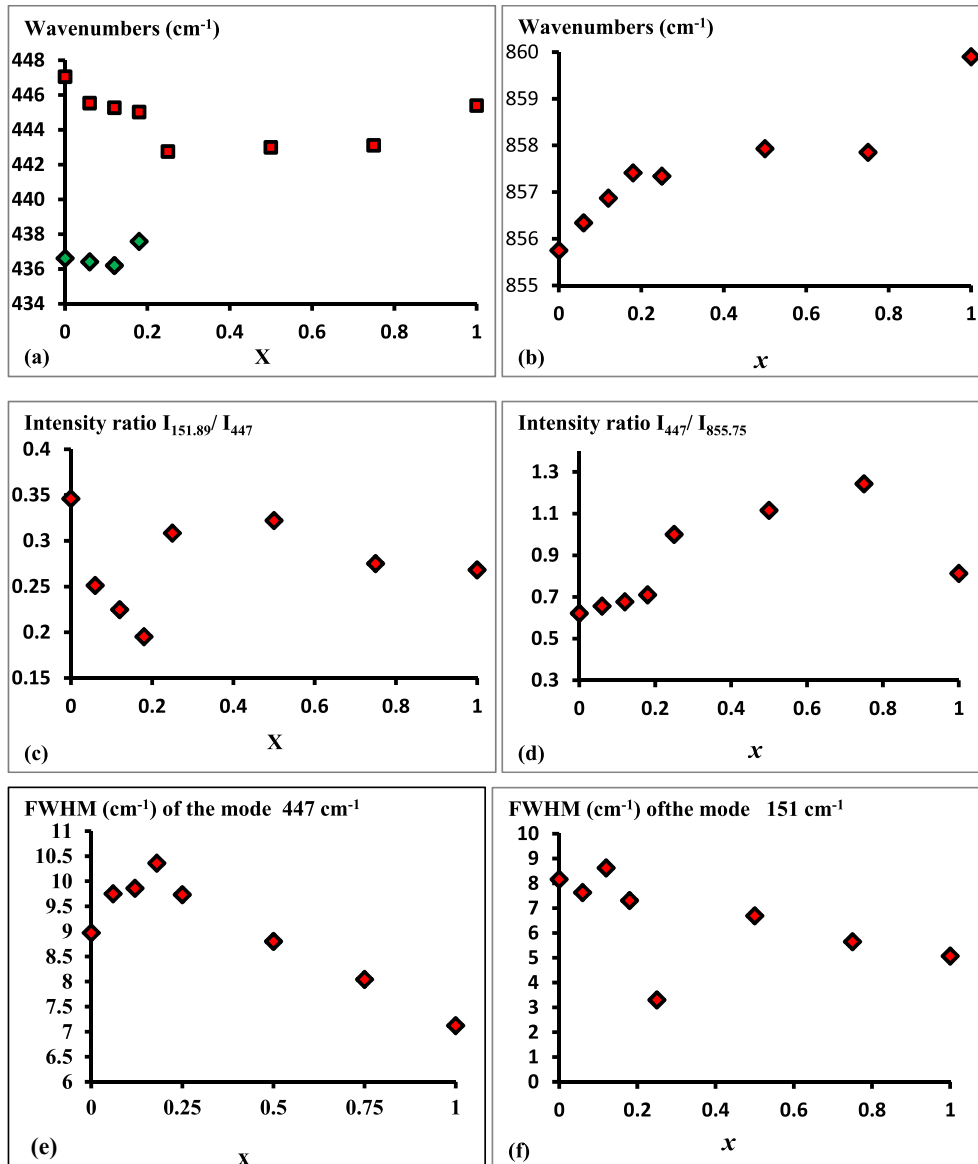


Fig. 8. Raman modes of $\text{Sr}_2\text{Zn}_{1-x}\text{Ni}_x\text{WO}_6$ vs. the composition x , the transition from the monoclinic phase to the tetragonal phase ($I4/m$) and from tetragonal phase ($I4/mmm$) shows considerable changes in the composition dependence of the modes.

$I4/mmm$ system, and the third from tetragonal symmetry $I4/mmm$ to cubic phase $Fm\bar{3}m$ at around 460°C . Also For the monoclinic $\text{Sr}_2\text{Zn}_{0.82}\text{Ni}_{0.18}\text{WO}_6$ two temperature phase transitions are observed at around 45°C and 450°C , respectively.

The tetragonal phase $\text{Sr}_2\text{Zn}_{0.75}\text{Ni}_{0.25}\text{WO}_6$ with $I4/m$ as space group have two phase transitions induced by temperature adopting the sequence $I4/m \rightarrow I4/mmm \rightarrow Fm\bar{3}m$. the temperature dependence of the mode centered at 856.81 cm^{-1} shows clear change in the slope at around 30°C indicating the first transition from tetragonal symmetry $I4/m$ to $I4/mmm$. Upon increasing temperature to 550°C , the second transition $I4/mmm \rightarrow Fm\bar{3}m$ is observed at around 445°C (Fig. 12a). The temperature dependence of ratio $M_{442.38\text{ cm}^{-1}}/M_{856.81\text{ cm}^{-1}}$ of the modes centered at 442.38 cm^{-1} and 856.81 cm^{-1} (Fig. 12b) shows clear changes in the slope at the same temperatures. The first change is revealed at 30°C and the second change is observed at around 445°C .

For tetragonal compounds with $I4/mmm$ the Raman spectra are also de-convoluted with "LABSPEC" program. Temperature induced the external and bending mode changes lead to a phase transition

from symmetry $I4/mmm$ to cubic $Fm\bar{3}m$ as presented in Fig. 13. For $\text{Sr}_2\text{Zn}_{0.5}\text{Ni}_{0.5}\text{WO}_6$, pronounced changes in the temperature dependence of the modes, are detected; the Raman modes ratio centered at 138 cm^{-1} and 858 cm^{-1} show a change in the slope at around 400°C , indicating the phase transition from the tetragonal ($I4/mmm$) to cubic ($Fm\bar{3}m$) structure (Fig. 13a). For $\text{Sr}_2\text{Zn}_{0.25}\text{Ni}_{0.75}\text{WO}_6$ the temperature dependence of Raman shift centered at 857.3 cm^{-1} show spectacularly change in slope indicating the transition to cubic system at around 340°C (Fig. 13b).

The temperature phase transition as a function of the composition is plotted in Fig. 14, the extrapolation of the curve shows that the composition induced phase transition is between $x = 0.18$ and $x = 0.25$ and between $x = 0.25$ and $x = 0.5$, thus confirming our Raman and X-ray diffraction results studied above.

4. Conclusions

The composition effects on the structural stability and phase transition of $\text{Sr}_2\text{Zn}_{1-x}\text{Ni}_x\text{WO}_6$ ($0 \leq x \leq 1$) have been studied using

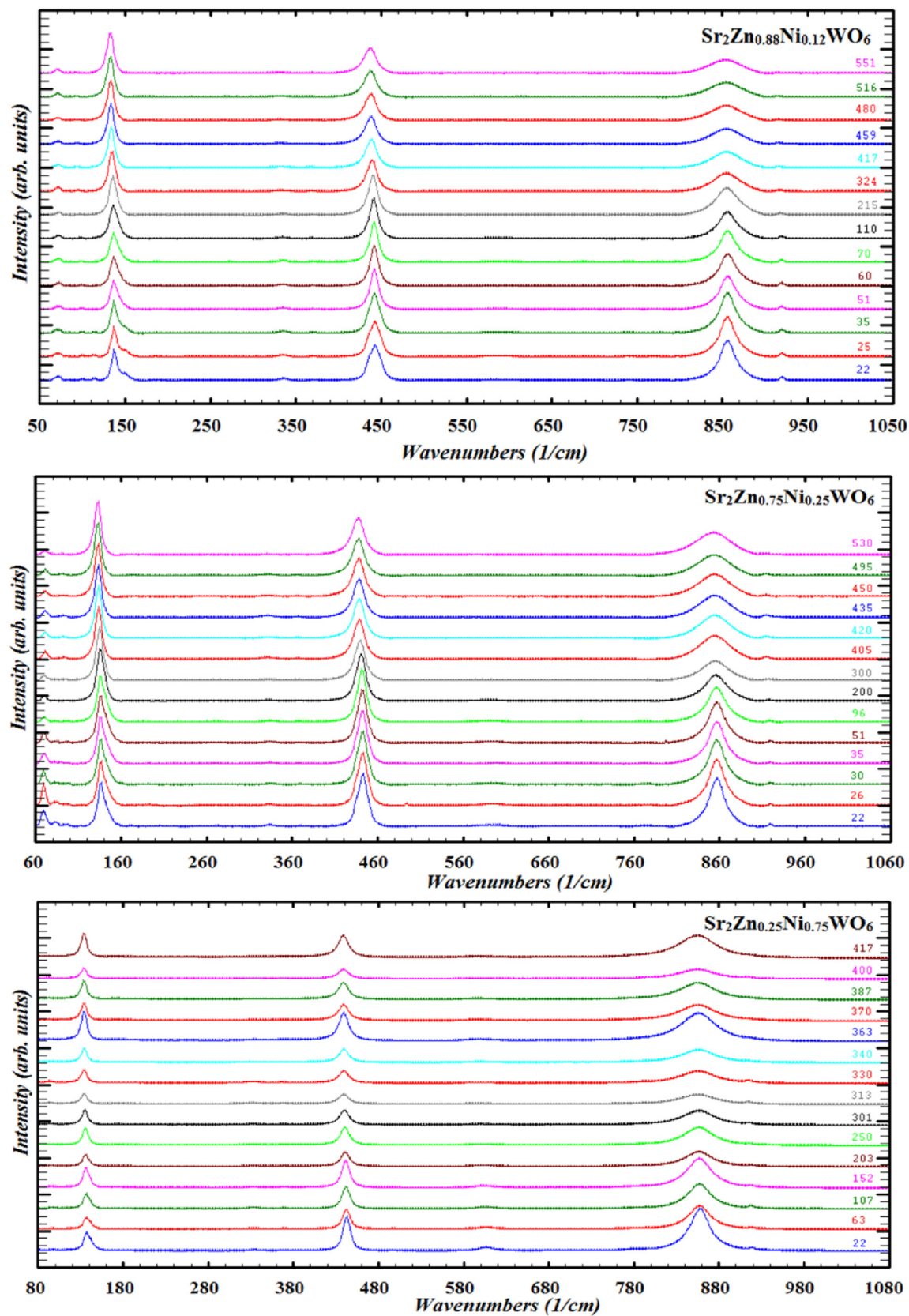


Fig. 9. Raman spectra of monoclinic compound $x = 0.12$, tetragonal compounds $x = 0.25$ and 0.75 obtained for selected temperatures, as indicated.

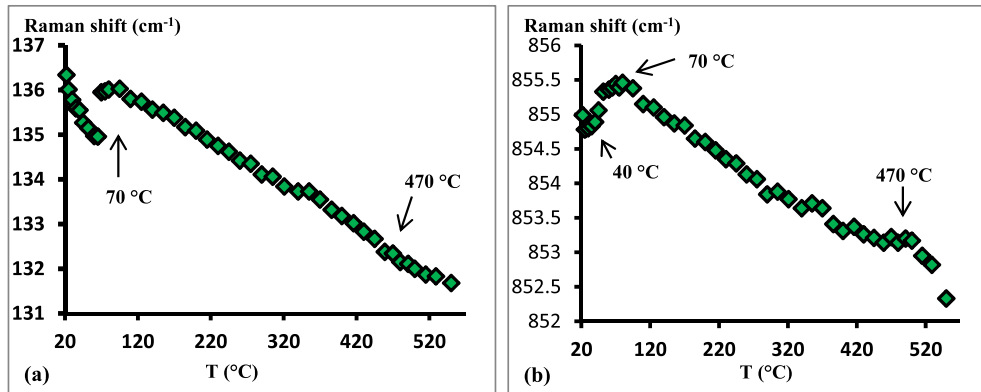


Fig. 10. Raman modes of $\text{Sr}_2\text{Zn}_{0.94}\text{Ni}_{0.06}\text{WO}_6$, vs. temperature. The temperature dependence of the modes centered at 136.34 cm^{-1} (a), 855 cm^{-1} (b) respectively.

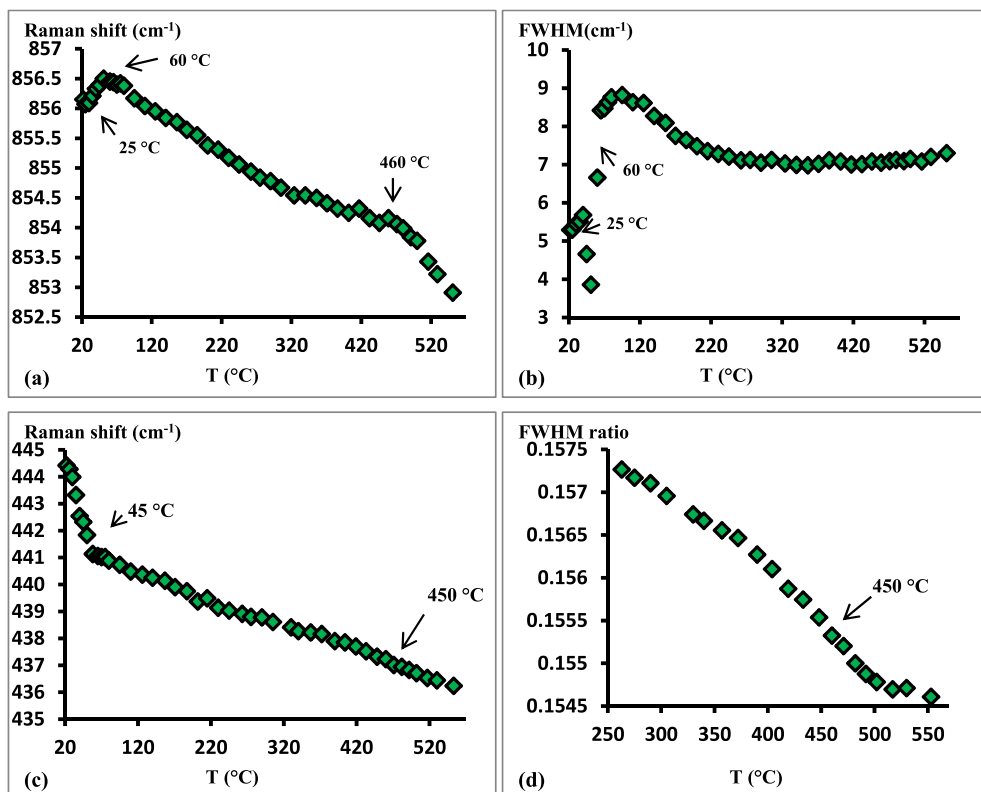


Fig. 11. Raman modes of $\text{Sr}_2\text{Zn}_{0.88}\text{Ni}_{0.12}\text{WO}_6$, vs. temperature. (a) Temperature dependence of the modes centered at 856.15 cm^{-1} . (b) Temperature dependence of the FWHM of the modes centered at 137 cm^{-1} and Raman modes of $\text{Sr}_2\text{Zn}_{0.82}\text{Ni}_{0.18}\text{WO}_6$, vs. temperature. (c) Temperature dependence of the modes centered at 444.42 cm^{-1} . (d) Temperature dependence of the FWHM ratio of the modes centered at 136 cm^{-1} and 855.37 cm^{-1} . The transition from one symmetry to another symmetry shows considerable changes in temperature dependence of the modes.

The X-ray powder diffraction and Raman spectroscopy techniques. The crystal structures were determined using the Rietveld refinements of laboratory X-ray powder diffraction data. With increasing the Ni composition, $\text{Sr}_2\text{Zn}_{1-x}\text{Ni}_x\text{WO}_6$ shows two phase transitions from monoclinic structure with the $P2_1/n$ space group for $0 \leq x \leq 0.18$ to tetragonal structure with the $I4/m$ space group for $x = 0.25$ and finally to tetragonal structure with the $I4/mmm$ space group for $0.5 \leq x \leq 1$. The high temperature Raman spectroscopy studies of the phase transitions in $\text{Sr}_2\text{Zn}_{1-x}\text{Ni}_x\text{WO}_6$ ($0 \leq x \leq 1$) double perovskite oxides show three phase transitions for monoclinic compounds $0 \leq x \leq 0.18$, the first from monoclinic $P2_1/n$ to tetragonal $I4/m$, the second from tetragonal $I4/m$ to tetragonal $I4/mmm$ and the third from tetragonal $I4/mmm$ to cubic $Fm\bar{3}m$.

For the tetragonal compound $\text{Sr}_2\text{Zn}_{0.75}\text{Ni}_{0.25}\text{WO}_6$, there are two phase transitions, the first from tetragonal $I4/m$ to tetragonal $I4/mmm$ and the second from tetragonal $I4/mmm$ to cubic $Fm\bar{3}m$ and finally for the tetragonal compounds with the compositions ranging between $0.5 \leq x \leq 1$ one phase transition is observed from tetragonal $I4/mmm$ to cubic $Fm\bar{3}m$.

We discovered four stable structural phases ($P2_1/n$, $I4/m$, $I4/mmm$, and $Fm\bar{3}m$) at different Ni content and temperature range, which provides key information on the structural stability and phase transition mechanism. Moreover, this is the first time to discover that $\text{Sr}_2\text{Ni}\text{WO}_6$ crystallizes with the space group $I4/mmm$, this space group is also adopted for Ni rich compositions. In fact when the pseudosymmetry search is restricted to the minimal

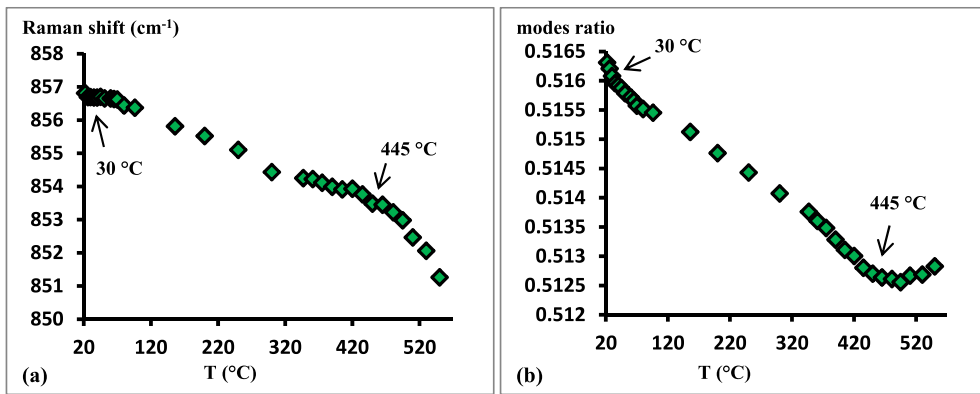


Fig. 12. Raman modes of $\text{Sr}_2\text{Zn}_{0.75}\text{Ni}_{0.25}\text{WO}_6$, vs. temperature. (a) temperature dependence of the mode centered at 856.81 cm^{-1} (b) temperature dependence of the ratio of the modes $(442.38 \text{ cm}^{-1})/(856.81 \text{ cm}^{-1})$.

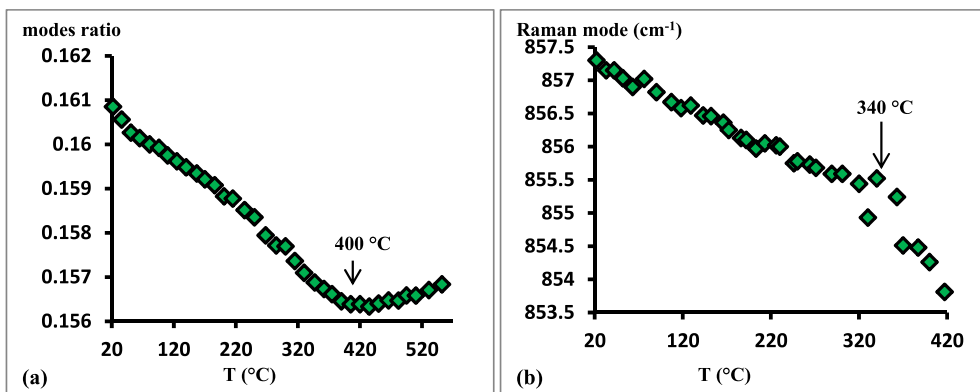


Fig. 13. Raman modes of $\text{Sr}_2\text{Zn}_{0.5}\text{Ni}_{0.5}\text{WO}_6$ and $\text{Sr}_2\text{Zn}_{0.25}\text{Ni}_{0.75}\text{WO}_6$, vs. temperature. (a) FWHM ratio of the mode centered at 442.97 cm^{-1} over 858 cm^{-1} of $\text{Sr}_2\text{Zn}_{0.5}\text{Ni}_{0.5}\text{WO}_6$. (b) Temperature dependence of the modes centered at 857.3 cm^{-1} of $\text{Sr}_2\text{Zn}_{0.25}\text{Ni}_{0.75}\text{WO}_6$.

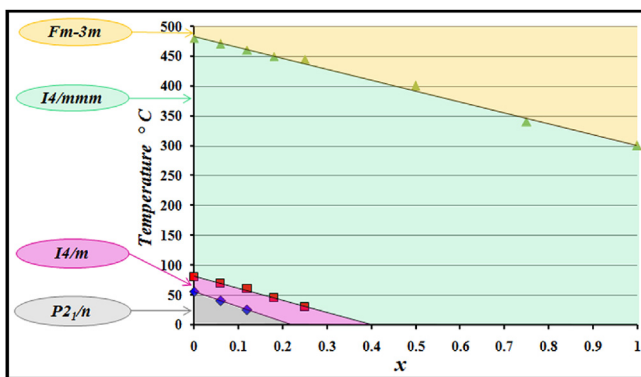


Fig. 14. Phase diagram of $\text{Sr}_2\text{Zn}_{1-x}\text{Ni}_x\text{WO}_6$ ($0 \leq x \leq 1$) as a function of the composition of nickel and temperature.

supergroups, the result obtained for $\text{Sr}_2\text{Ni}\text{WO}_6$ is that it has pseudosymmetry with the *I4/mmm* space group. It should be pointed out that, for the case of double perovskite structures with *I4/m* space group, *I4/mmm* is the only minimal supergroup that can be accessed with displacements of the atoms.

Our combined study on the structural evolution by the XRD and Raman spectroscopy measurements as a function of composition and or temperature provides a comprehensive understanding of this type of double perovskite from the lattice, bond strength, and vibrational points of view. We expect that these materials will be of great interest in electric transport field.

Acknowledgements

The authors are grateful to the University Hassan 1st and the Swedish Research Council for the financial grant 348-2014-4287, Swedish Research Links.

References

- [1] A.W. Sleight, J.L. Gillson, P.E. Bierstedt, High-temperature superconductivity in the $\text{BaPb}_{1-x}\text{Bi}_x\text{O}_3$ systems, Solid State Commun. 17 (1975) 27.
- [2] E. Cox, A.W. Sleight (Eds.), Proceedings of the Conference on Neutron Scattering, National Technical Information Service, U.S. Department of Commerce, Springfield, Virginia, 1976, p. 45.
- [3] M.A. Akbas, P.K. Davies, Ordering-induced microstructures and microwave dielectric properties of the $\text{Ba}(\text{Mg}_{1/3}\text{Nb}_{2/3})\text{O}_3\text{-BaZrO}_3$ system, J. Am. Ceram. Soc. 81 (1998) 670.
- [4] I.M. Reaney, E.L. Colla, N. Setter, Dielectric and structural characteristics of Ba- and Sr-based complex perovskites as a function of tolerance factor, Jpn. J. Appl. Phys. 33 (1994) 3984.
- [5] K.-I. Kobayashi, T. Kimura, H. Sawada, K. Terakura, Y. Tokura, Room-temperature magnetoresistance in an oxide material with an ordered double-perovskite structure, Nat. Lond. 395 (1998) 677.
- [6] P.M. Woodward, Octahedral tilting in perovskites. I, Geom. Consid. Acta Crystallogr. B 53 (1997) 32.
- [7] C.J. Howard, B.J. Kennedy, P.M. Woodward, Ordered double perovskites - a group-theoretical analysis, Acta Crystallogr. 59 (2003) 463.
- [8] A.P.J. Ramirez, Colossal magnetoresistance, Phys. Condens. Matter 9 (1997) 8171.
- [9] C.N.R. Rao, B. Raveau (Eds.), Colossal Magnetoresistance, Charge Ordering and Related Properties of Manganese Oxides, World Scientific, Singapore, 1998.
- [10] J.B. Philipp, P. Majewski, L. Alff, A. Erb, R. Gross, T. Graf, M.S. Brandt, J. Simon, T. Walther, W. Mader, D. Topwal, D.D. Sarma, Structural and doping effects in the half-metallic double perovskite $\text{A}_2\text{Cr}\text{WO}_6$ ($\text{A}=\text{Sr}, \text{Ba}, \text{and Ca}$), Phys. Rev. B 68 (2003) 144431.

- [11] F. Zhao, Z.X. Yue, Z.L. Gui, L.T. Li, Preparation, characterization and microwave dielectric properties of A_2BW_6 ($A = Sr, Ba; B=Co, Ni, Zn$) double perovskite ceramics, *Jpn. J. Appl. Phys.* 44 (2005) 8066.
- [12] G. Popov, M. Greenblatt, M. Croft, Large effects of A-site average cation size on the properties of the double perovskites $Ba_{2-x}Sr_xMnReO_6$: A d^5-d^1 System, *Phys. Rev. B* 67 (2003) 024406.
- [13] A. Maingan, B. Raveau, C. Martin, M. Hervieu, Large intragrain magnetoresistance above room temperature in the double perovskite Ba_2FeMoO_6 , *J. Solid State Chem.* 144 (1999) 224.
- [14] K.-I. Kobayashi, T. Kimura, Y. Tomioka, H. Sawada, K. Terakura, Y. Tokura, Intergrain tunneling magnetoresistance in polycrystals of the ordered double perovskite Sr_2FeReO_6 , *Phys. Rev. B* 59 (1999) 11159.
- [15] J.A. Alonso, M.T. Casais, M.J. Martínez-Lope, J.L. Martínez, P. Velasco, A. Muñoz, M.T. Fernández Diaz, Preparation, crystal structure, and magnetic and magnetotransport properties of the double perovskite Ca_2FeMoO_6 , *Chem. Mater.* 12 (2000) 161.
- [16] M. Gateshki, J.M. Igartua, E. Hernandez-Bocanegra, X-ray powder diffraction results for the phase transitions in Sr_2MW_6 ($M = Ni, Zn, Co, Cu$) double perovskite oxides, *J. Phys. Cond. Matter* 15 (2003) 6199–6217.
- [17] M. Gateshki, J.M. Igartua, Crystal structures and phase transitions of the double-perovskite oxides Sr_2CaWO_6 and Sr_2MgWO_6 , *J. Phys. Condens. Matter* 16 (2004) 6639–6649.
- [18] Daisuke Iwanaga, Yoshiyuki Inaguma, Mitsuru Itoh, structure and magnetic properties of Sr_2NiAO_6 ($A = W, Te$), *Mater. Res. Bull.* 35 (2000) 449–457.
- [19] S.Z. Tian, J.C. Zhao, C.D. Qiao, X.L. Ji, B.Z. Jiang, Structure and properties of the ordered double perovskites Sr_2MW_6 ($M = Co, Ni$) by sol-gel route, *Mater. Lett.* 60 (2006) 2747–2750.
- [20] M.F. Kupriyanov, E.G. Fesenko, X-ray structural studies of phase transitions in perovskite-type compounds, *Krist* 7 (1962) 451.
- [21] D. Reinen, H.O. Wellner, Wegwerth, Jahn-teller-type phase transitions in oxide ceramics and other solids with Cu(II)—From the viewpoint of a solid state chemist, *J. Z. Phys. B* 104 (1997) 595.
- [22] Bouchaib Manoun, Josu M. Igartua, Peter Lazor, Amine Ezzahi, High temperature induced phase transitions in Sr_2ZnW_6 and Sr_2CoWO_6 double perovskite oxides: Raman spectroscopy as a tool, *J. Mol. Struct.* 1029 (2012) 81–85.
- [23] Bouchaib Manoun, Josu M. Igartua, Peter Lazor, High temperature Raman spectroscopy studies of the phase transitions in Sr_2NiWO_6 and Sr_2MgWO_6 double perovskite oxides, *J. Mol. Struct.* 971 (2010) 18–22.
- [24] J. Rodriguez-Carvajal, Recent advances in magnetic structure determination by neutron powder diffraction, *Phys. B* 192 (1993) 55.
- [25] T. Roisnel, J. Rodriguez-Carvajal, WinPLOT: a windows tool for powder diffraction pattern analysis, *Mater. Sci. Forum* 378–381 (2001) 118.
- [26] M. Azdouz, B. Manoun, M. Azrour, L. Bih, L. El Ammar, S. Benmokhtar, P. Lazor, Synthesis, Rietveld refinements and Raman spectroscopy studies of the solid solution $Na_{1-x}K_xPb_4(VO_4)_3$ ($0 < x < 1$), *J. Mol. Struct.* 963 (2010) 258.
- [27] H. Bih, L. Bih, B. Manoun, M. Azdouz, S. Benmokhtar, P. Lazor, Raman spectroscopic study of the phase transitions sequence in $Li_3Fe_2(PO_4)_3$ and $Na_3Fe_2(PO_4)_3$ at high temperature, *J. Mol. Struct.* 936 (2009) 147–155.
- [28] R.D. Shannon, Revised effective ionic radii and systematic studies of interatomic distances in halides and chalcogenides, *Acta Cryst. A* 32 (1976) 751–767.
- [29] Bradley E. Day, Nicholas D. Bley, Heather R. Jones, Ryan M. McCullough, Hank W. Eng, Spencer H. Porter, Patrick M. Woodward, Paris W. Barnes, Structures of ordered tungsten- or molybdenum-containing quaternary perovskite oxides, *J. Solid State Chem.* 185 (2012) 107–116.
- [30] W.T. Fu, S. Akerboom, D.J.W. IJdo, The intermediate tilt systems in the double perovskites $Ba_{1-x}Sr_xCaW_6$ and $Ba_{2-x}Sr_xYSbO_6$, *J. Alloys Compd.* 476 (2009) L11–L15.
- [31] Y.P. Liu, S.H. Chen, H.R. Fuh, Y.K. Wang, First-principle calculations of half-metallic double perovskite $La_2BB' O_6$ ($B, B'=3d$ transition metal), *Commun. Comput. Phys.* 14 (2013) 174–185.
- [32] A.M. Glazer, Simple ways of determining perovskite structures, *Acta Cryst. A* 31 (1975) 756.
- [33] E. Kroumová, M.I. Aroyo, J.M. Perez-Mato, A. Kirov, C. Capillas, S. Ivantchev, H. Wondratschek, Bilbao Crystallographic Server: useful databases and tools for phase transitions studies, *Phase Transit* 76 (2003) 155. <http://www.cryst.ehu.es/>.
- [34] M. Liegeois-Duyckaerts, P. Tarte, Vibrational studies of molybdates, tungstates and related c compounds—III. Ordered cubic perovskites $A_2B^{II}B^{VI}>O₆, *Spectrochim. Acta, Part A* 30 (1974) 1771–1786.$
- [35] A.P. Ayala, I. Guedes, E.N. Silva, M.S. Augsburger, M. del C. Viola, J.C. Pedregosa, Raman investigation of A_2CoBO_6 ($A = Sr$ and Ca, B = Te and W) double perovskites, *J. Appl. Phys.* 101 (2007) 123511.
- [36] Anderson Dias, Ganeshapotti Subodh, Mailadil T. Sebastianb, Roberto L. Moreira, Vibrational spectroscopic study of Sr_2ZnTeO_6 double perovskites, *J. Raman Spectrosc.* 41 (2010) 702–706.
- [37] Q. Zhou, B.J. Kennedy, M.M. Elcombe, Composition and temperature dependent phase transitions in Co–W double perovskites, a synchrotron X-ray and neutron powder diffraction study, *J. Solid State Chem.* 180 (2007) 541.
- [38] Frank Herman, Robert V. Kasowski, Y. William, Hsu Electronic structure of $Bi_2Sr_2CaCu_2O_8$ high Tc superconductors, *Phys. Rev. B* 38 (1) (1988) 204–207.
- [39] M.K. Wu, D.Y. Chen, F.Z. Chien, S.R. Sheen, D.C. Ling, C.Y. Tai, G.Y. Tseng, D.H. Chen, F.C. Zhang, Anomalous magnetic and superconducting properties in a Ru-based double perovskite, *Z. Phys. B* 102 (1997) 37–41.
- [40] S.M. Rao, J.K. Srivastava, H.Y. Tang, D.C. Ling, C.C. Chung, J.L. Yang, S.R. Sheen, M.K. Wu, Crystal growth of a new superconducting double perovskite $A_2YRu_{1-x}Cu_xO_6$ ($A = Ba, Sr$), *J. Cryst. Growth* 235 (2002) 271–276.
- [41] Mirza H.K. Rubel, Akira Miura, Takahiro Takei, Nobuhiro Kumada, M. Mozahar Ali, Masanori Nagao, Satoshi Watauchi, Isao Tanaka, Kengo Oka, Masaki Azuma, Eisuke Magome, Chikako Moriyoshi, Yoshihiro Kuroiwa, A.K.M. Azharul Islam, Superconducting double perovskite bismuth oxide prepared by a low-temperature hydrothermal reaction, *Angew. Chem. Int. Ed.* 53 (2014) 3599–3603.
- [42] Bouchaib Manoun, Y. Tamraoui, P. Lazor, Wenge Yang, Phase transitions in heated Sr_2MgTeO_6 double perovskite oxide probed by X-ray diffraction and Raman spectroscopy, *Appl. Phys. Lett.* 103 (2013) 261908.
- [43] Milen Gateshki, Josu M. Igartua, Second-order structural phase transition in Sr_2CuWO_6 double-perovskite oxide, *J. Phys. Condens. Matter* 15 (2003) 6749–6757.